Flutter predictions for very flexible wing wind tunnel test*

Norberto Goizueta†, Andrew Wynn‡ and Rafael Palacios§
Department of Aeronautics, Imperial College London, SW7 2AZ

Ariel Drachinsky¶ and Daniella E. Raveh‖
Faculty of Aerospace Engineering, Technion - IIT, Israel

The stability boundaries of a very flexible wing are sought to inform a wind-tunnel flutter test campaign. The objective is twofold: to identify via simulation the relevant physical processes to be explored while ensuring safe and non-destructive experiments, and to provide a benchmark case for which computational models and test data are freely available. Analyses have been independently carried out using two geometrically nonlinear structural models coupled with potential flow aerodynamics. The models are based on a prototype of the wing for which static load and aeroelastic tests are available, and the experimental results have been successfully reproduced numerically. The wing displays strong geometrically nonlinear effects with static deformations as high as 50% of its span. This results in substantial changes to its structural dynamics, which display several mode crossings that cause the flutter mechanisms to change as a function of deformation. Stability characteristics depend on both the free-stream velocity and the angle of attack. A fast drop of the flutter speed is observed as the wing deforms as the angle of attack is increased, while a large stable region is observed for wing displacements over 25%. The corresponding wind tunnel dynamic tests have validated these predictions.

I. Introduction

Flutter clearance is a well-established process and a basic feature in aircraft design [1, 2]. For conventional (and many unconventional) vehicles, the aeroelastic stability boundary can be well predicted using the natural vibration modes of the undeformed structure and linear unsteady aerodynamics (traditionally obtained using the Doublet-Lattice Method corrected using wind tunnel or high-fidelity aerodynamic simulation data). Aerodynamic loading however creates a follower force on the deforming structure which requires updating the aerodynamic computational mesh. In some situations, such as T-tails at non-zero incidence angle, steady aerodynamics may also play an important (and

*This paper was originally presented as Paper No. 2021-1711 at the AIAA 2021 SciTech Forum, Virtual event, 11-15 & 19-21 January 2021.
†PhD Student, CAGB 308, South Kensington Campus. (norberto.goizueta13@imperial.ac.uk)
‡Reader in Control and Optimization, CAGB 340, South Kensington Campus. (a.wynn@imperial.ac.uk)
§Professor of Computational Aeroelasticity, CAGB 338, South Kensington Campus. AIAA Associate Fellow (corresponding author - r.palacios@imperial.ac.uk)
¶PhD Student, Faculty of Aerospace Engineering, Technion, Haifa 32000. (arikdra@gmail.com)
‖Professor, Faculty of Aerospace Engineering, Technion, Haifa 32000. AIAA Associate Fellow (daniella@technion.ac.il)

destabilizing) role in the basic flutter mechanism [3, 4]. Further complications may be encountered with very flexible wings, where the change in geometric stiffness and moments of inertia resulting from wing deformation modify the vibration characteristics, and may have a large effect on the onset of flutter [5]. For the gust load evaluation problem of high aspect ratio wings, it is also crucial not only to account for these steady loads, but also to use the deformed trim geometry as linearization reference given the effect on loads and flight dynamic modes [6].

Very flexible wings have been long considered for power-constrained vehicles, such as solar-powered aircraft, which seek large aerodynamic efficiency with very lightweight structures. The former leads to designs with very high aspect ratio, that, when coupled with modern lightweight materials, result in wings that are capable of achieving wingtip deflections comparable to their span. Very high aspect ratio wings, also susceptible to large deformations, are also considered in most future concepts of ultra-low (or zero) emission commercial transport aircraft [7]. The large deformations induced by the aerodynamic forces make it indispensable to design the system with an aeroelastic perspective, with tools and methods capable of capturing geometrically-nonlinear structural effects [8, 9]. Since a basic feature of these vehicles is the presence of very high aspect ratio wings, one-dimensional beam approximations are an attractive alternative for the structural model. In addition, the mostly-attached nature of the flow at low wing-sections angles of attack and the prevalence of thin lifting surfaces make potential flow based aerodynamics a viable option below transonic speeds, provided it can still accommodate large wing displacements [10].

Most recent work on high aspect ratio very flexible wings employs similar methods [11, 12] and shares common focus to this paper in the prediction of the flutter onset of said aeroelastic systems, for which a thorough review of flutter and post-flutter prediction methods can be found in Ref. [13]. For instance, for the large aspect ratio truss-braced wing, Refs. [14, 15] use transonic wind tunnel data to explore wing and engine nacelle limit cycle oscillations for concepts like the Boeing SUGAR or NASA TBW. In the particular case of the Boeing SUGAR, the second out-of-plane bending and the first torsional mode coalesce, where the onset of instability is a function of the aircraft's angle of attack (similar to the case study shown in this work) [14]. Predicting post-flutter behavior is also of great importance, since nonlinearities can cause divergent flutter modes to stabilize into limit cycle oscillations (LCO), and although post-flutter is not within the scope of this work, the reader is referred to Ref. [16] for novel and efficient data-driven methods to predict LCOs large aspect ratio wings with geometrically nonlinear effects. Note, finally, that the characteristics of the LCOs may be strongly affected by nonlinearities in structural damping but the topic of damping has been explored extensively for the F16 wing stores in Refs. [17–19].

However, as with all computational methods, the question remains as to how accurate are they and whether they are able to capture all the key physical phenomena. In other words, whether they are valid [20] in modeling and simulating the aeroelastic response of slender, flexible lifting bodies. Few aeroelastic benchmark cases for which experimental data is available exist and thus most comparisons between methods have been purely numerical [21]. In terms of experimental flutter data sets, we find, dating back to the 80's, Dugundji's work on swept, composite wings, which includes nonlinear

aerodynamic effects [22, 23], as well as the Duke University wing [24–27], dating from 2001. However, limited data is available and corresponds to a few angles of attack and deformations below 20% of span. Later, an extensive and thorough wind tunnel test campaign on a DARPA Vulture-inspired cantilever wing was carried out in 2012 to validate the nonlinear aeroelastic methods used in the project [28]. Despite the extensive data presented and the interesting aeroelastic phenomena exhibited by the wing, its complex geometry (with several horizontal and vertical surfaces) likely does not make it an ideal candidate for its use by the wider aeroelastic community in validating their own tools. Most recently, a novel benchmark case has been presented at the Technion [29] of a very flexible clamped wing, designed to undergo deformations beyond 50% of span and to be used for flutter tests in the wind tunnel. This wing, named the Pazy wing, consists of an aluminum spar and a Nylon chassis (consisting of evenly-spaced NACA0018-shaped ribs and a wing tip rod). To give it the external aerodynamic shape, the wing is covered with an Oralight polyester skin. The Pazy wing is a bespoke wing built specifically for this purpose, but in the case of large scale wings replicated for wind tunnel analysis, Ref. [30] explores the important topic of deriving adequately scaled models that display similar aeroelastic phenomena as their full sized counterparts.

This paper has two objectives. First, to showcase the importance of geometrical nonlinearities in the flutter prediction of very flexible wings by comparing and assessing the performance of two aeroelastic solution methods, described briefly in Sec. II, against a prototype of the wing. The wing is thoroughly described in Sec. III alongside the relevant approximations used in the models. Section IV compares the numerical models with the static experimental results, which serve as a model validation exercise. Thence, the dynamic aeroelastic behavior is discussed in Sec. V, where the flutter boundary of the wing is analyzed for different root angles of attack simulating the conditions in the wind tunnel. The result is the aeroelastic stability envelope of the wing as a function of free-stream velocity, angle of attack and deformation which has been used for the design of an experimental flutter test. The first available wind-tunnel test results validate the proposed methodologies in the prediction of the nonlinear flutter boundary and are summarized in Sec. V.D.

The second objective is to use the Pazy wing case as a benchmark case for the comparison and validation of future aeroelastic tools and experiments. This is within the scope of the Large Deflection working group of NASA's 3rd Aeroelastic Prediction Workshop (AePW3) which aims to bring together different numerical and experimental knowledge from academia to solve relevant and modern aeroelastic problems. For such a purpose, we provide all models, scripts and codes used to obtain the results presented herein available as open source. Details on how to obtain them can be found in the Appendix.

II. Numerical Methods

Two computational methods were used with different structural and aerodynamic models which are tailored for aeroelastic applications such as the one at hand. Thus, this section will provide a brief summary and direct the reader to the appropriate references for further detail.

A. SHARPy

SHARPy (Simulation of High Aspect Ratio airplanes and wind turbines in Python) is a nonlinear aeroelastic simulation toolbox available under open-source license [31]. At its core, SHARPy couples a geometrically-nonlinear composite beam solver with a potential-flow unsteady aerodynamic model with sectional corrections. It also includes a consistent analytical linearization of these nonlinear models around arbitrary static aeroelastic equilibria [32] and several implementations of model-order reduction methods [33, 34]. SHARPy has tens of modules that can be combined for specific analysis and interested readers can find details in the extensive online documentation [35]. For brevity, we will only summarize here those modules that need to be employed to compute flutter of highly-flexible, clamped structures. For this we will (i) solve for the geometrically-nonlinear static aeroelastic equilibrium condition of the wing at a given angle of attack and free-stream velocity; (ii) linearize the structural and aerodynamic systems about this deformed configuration; (iii) reduce the systems using modal reduction and Krylov-based methods, respectively; and (iv) analyze the stability of the resulting reduced linear state-space.

The structural model is based on a geometrically-exact 1D beam formulation, with linear constitutive relations and nonlinear velocity and displacement kinematic relations. The formulation is parametrized in displacements and rotations and applied by discretizing the beam in quadratic (3-node) finite elements [36, 37]. The nonlinear equations that result from the application of Hamilton's principle take the form of [21]

$$\boldsymbol{\mathcal{M}}(\boldsymbol{\eta})\ddot{\boldsymbol{\eta}} + \boldsymbol{Q}_{\text{gyr}}(\boldsymbol{\eta}, \dot{\boldsymbol{\eta}}) + \boldsymbol{Q}_{\text{stiff}}(\boldsymbol{\eta}) = \boldsymbol{Q}_{\text{ext}}(\boldsymbol{\eta}, \dot{\boldsymbol{\eta}}), \tag{1}$$

where $\boldsymbol{\mathcal{M}}$ is the mass matrix and $\boldsymbol{Q}$ represents the discrete external (aerodynamic), gyroscopic and stiffness forces. The flexible degrees of freedom expressed in a body-attached frame, $\boldsymbol{\eta} \in \mathbb{R}^{6\times(n_{\text{nodes}}-1)}$, include nodal displacements and rotations, the latter parametrized through a Cartesian rotation vector (CRV).

These equations are then linearized about a reference equilibrium condition, defined, in general, by the constant values $(\boldsymbol{\eta}_0, \dot{\boldsymbol{\eta}}_0)$ and with $\ddot{\boldsymbol{\eta}}_0 = \mathbf{0}$. Using δ to indicate small perturbations, this results in [32]

$$\boldsymbol{\mathcal{M}}(\boldsymbol{\eta}_0)\delta\ddot{\boldsymbol{\eta}} + \boldsymbol{C}(\boldsymbol{\eta}_0, \dot{\boldsymbol{\eta}}_0)\delta\dot{\boldsymbol{\eta}} + \boldsymbol{\mathcal{K}}(\boldsymbol{\eta}_0, \dot{\boldsymbol{\eta}}_0)\delta\boldsymbol{\eta} = \delta\boldsymbol{Q}_{ext}(\delta\boldsymbol{\eta}, \delta\dot{\boldsymbol{\eta}}), \tag{2}$$

where $\boldsymbol{C}$ and $\boldsymbol{\mathcal{K}}$ are the tangent damping and tangent stiffness matrices, respectively. The system can then be projected onto modal coordinates (which will depend on the equilibrium shape) and truncated to retain the modes that capture the most significant dynamics.

In SHARPy, the aerodynamics are solved using an Unsteady Vortex Lattice Method (UVLM), which is based on the assumptions of incompressible potential-flow theory [10, 21, 38, 39]. Vortex panels are laid out over lifting surfaces, with their spanwise location coincident with that of the underlying structural elements. In turn, the wake can be modeled

by either infinitely long horseshoe vortices (in static simulations) or with discrete panels that are influenced by the bound and other wake vortices (for unsteady simulations). The flow field itself is solved enforcing the non-penetration boundary condition at the center of the bound vortex rings by adjusting their circulation strength. The formulation is nonlinear given the dependency of the aerodynamic influence coefficients (which contain the information on how each vortex affects others) on the instantaneous deformation of the structure and shape of the wake sheet. Once the circulation of the vortices has been solved for, the aerodynamic forces are calculated attending to steady and unsteady contributions: the steady forces are calculated using the Joukowsky theorem [40] whereas for the unsteady forces we use Bernoulli's unsteady equation based on the time derivative of the circulation, which is calculated by finite differences. An important underlying assumption is that all viscous effects are confined to thin boundary layers whose effects can be neglected, including viscous drag contributions and flow separation [10]. Stall has not been modeled in the results presented in this work.

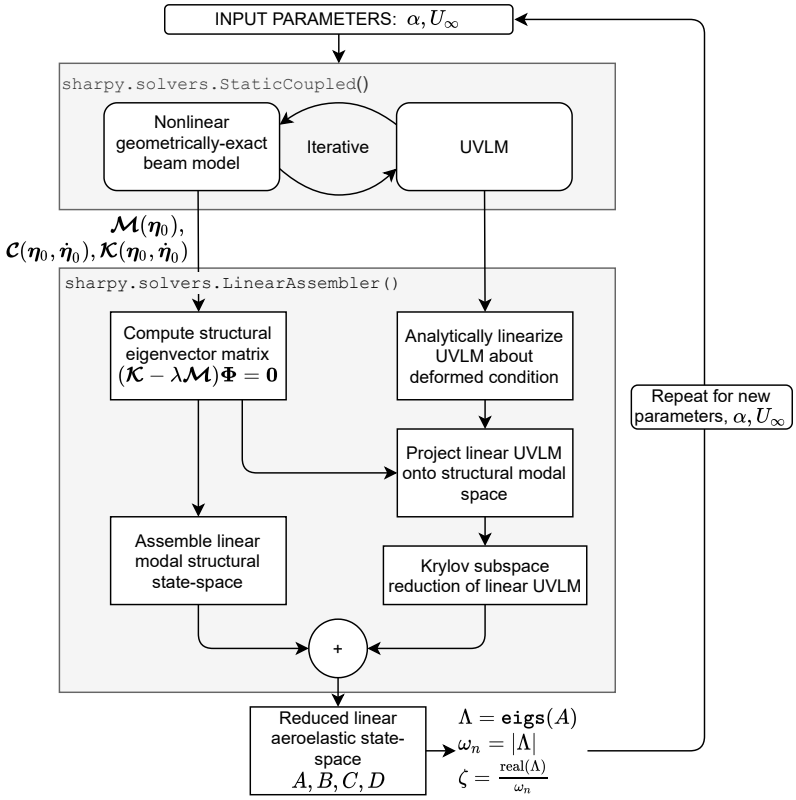

Fig. 1 SHARPy solution process to obtain frequency and damping data for each angle of attack and free stream velocity pair.

The linearization of the UVLM equations is performed analytically about the deformed equilibrium shape under the assumption of a frozen, yet arbitrary (i.e. including wake roll-up), wake shape [41]; the linearization includes steady load effects [3] which appear as a result of non-zero aerodynamic loading at the reference condition and are

treated as follower forces. To achieve numerical convergence and capture unsteady effects a highly resolved bound vortex lattice and a long wake are typically required [33, 41, 42], so it is highly convenient to reduce the system to alleviate the computational burden of linear analysis tools, such as computing the system's eigenvalues. Thus, we turn to Krylov subspace methods to reduce the dimension of the aerodynamic system [34]. This is a computationally efficient model order reduction method based on matching the transfer functions and their derivatives at user-defined frequencies, which for aeroelastic problems we limit to the lower end of the spectrum [10]. Nonetheless, since this reduction method is based on transfer function matching, the reduced order system is prone to be of significant size if the input/output dimensionality is large. This is the case of the linear UVLM, where the inputs (displacement and velocities) and outputs (forces) are defined at each of the lattice vertices. Therefore, under the assumption of chordwise rigid rotations about the beam elements, the UVLM input/output space is projected onto the modal coordinates of the underlying beam element, which significantly reduces the dimensionality. Then, the Krylov subspace reduction can be performed efficiently, leading to substantial model size reductions: full order, converged UVLM systems for a full vehicle are typically in the range of $O(10^5)$ states and they are reduced to $O(10)$ states.

The coupling between the linear structural and aerodynamic models is trivial, since the inputs and outputs of both systems are expressed in the structural modal coordinates. The aeroelastic system is also of a sufficiently small size that stability (by computing the system eigenvalues) and other linear analyses can be performed very efficiently.

The stability properties of the wing are then computed by finding the eigenvalues of the linearized system matrix for each combination of the test parameters (namely angle of attack, α, and free stream velocity, U_∞) to find the aeroelastic modes damping and frequency characteristics, which will be used to define the flutter envelope. A schematic of this solution process is shown in Fig. 1 and the linearized system is recomputed at each condition given the changes introduced into the structural and aerodynamic systems by the large deflections.

B. Modal Rotation Method

A static mathematical model of the Modal Rotation Method (MRM) has been presented in Ref. [43], and was recently extended for a dynamic aeroelastic solution in Ref. [44]. It is developed for computing nonlinear large deformations of flexible, *slender* structures. While the MRM is not limited to analyzing beams, it solves the structural deformations along a *reference line*. For wing structures, this line runs over the wing-span, typically along the mid-chord, the leading or trailing-edge. The modes are described in segments over the reference line. The segmentation and reference line concepts are illustrated in Fig. 2. The MRM formulation is based on *curvature* mode shapes that are computed in a free-vibration analysis from a linear finite-element model. The curvature modes are interpolated to segments along the reference line. Provided that this line is divided into sufficiently small segments, the change in the rotation in each

segment is small. This allows for a linearized, modal based evaluation of the rotation change in each segment:

$$\{d\theta\} = [\phi_{d\theta}]\{\xi\} \tag{3}$$

and their summation over the structure (over the reference line) using nonlinear kinematics:

$$\{U_i\} = \{U_{i-1}\} + [R_i]\{dl_i\} \tag{4}$$

where $\{d\theta\}$ is a vector of angle changes (curvatures), $[\phi_{d\theta}]$ is a matrix of curvature mode shapes, $\{U_i\}$ is a displacement vector, and $[R_i]$ is a rotation matrix of the i-th segment which is based on the summation of the local curvatures (represented via Euler angles) from the root to the segment. To accurately model the internal bending moments, the MRM applies an iterative procedure that updates the location and orientation of the applied external loads based on the deformed shape via external correction moments:

$$\{\Delta M_i\} = \{M_{\mathrm{loc}_i}\} - \{M_{0i}\} - \sum_{j=i+1}^{n} \{\Delta M_j\} \tag{5}$$

where $\{M_{\mathrm{loc}_i}\}$ is the internal moment in the deformed configuration $\{M_{0i}\}$ is the internal moment acting on the undeformed configuration and n the total number of segments.

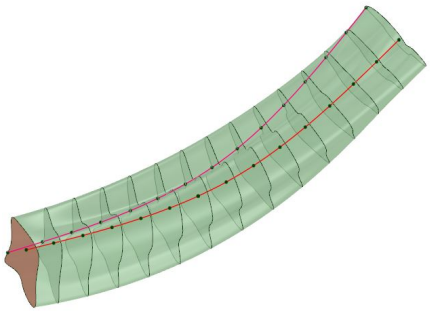

Fig. 2 Illustration of the segmentation and two arbitrary reference lines used in the MRM [43].

The MRM is coupled with an aerodynamic model, based on the rigid configuration, to compute static aeroelastic deformations and the flutter velocity about the static equilibrium. Two methods are proposed to update the structural data of the deformed structure, alter the unsteady aerodynamic matrices, and obtain a flutter solution for the deformed wing. One is based on the discrete mass and aerodynamic properties of the wing and the other only on modal data, thus providing a nonlinear solution that is based only on linear modal data. The curvature-based representation yields a generalized stiffness matrix that does not change with the deformation [45]. Updating the generalized mass matrix is

done by representing the deformed mode shapes as a combination of the baseline mode shapes

$$[\phi_{\text{def}}] \approx [\phi]\,[G]\,, \tag{6}$$

This yields an expression for the deformed generalized mass matrix that is based directly on the modal mass matrix of the undeformed structure:

$$[GM_{\text{def}}] = \underbrace{[G^\top][\phi^\top]}_{[\phi_{\text{def}}^\top]}[M]\,\underbrace{[\phi][G]}_{[\phi_{\text{def}}]} = [G^\top][GM][G] \tag{7}$$

where $[GM] = [\phi]^\top[M][\phi]$. For the update of the deformed aerodynamic matrices, we assume that the relation between local incremental angle of attack and the local forces does not change with large deformation. This is equivalent to the strip theory assumption that the local strip characteristics are unaffected by the deformation, although we note that the baseline model does not have to be generated by a strip theory. Under this assumption, updating the aerodynamic matrix is done similarly to the update of the mass matrix, yielding:

$$[Q_{HH,\text{def}}(ik)] = \underbrace{[G^\top][\phi^\top]}_{[\phi_{\text{def}}^\top]}[AIC(ik)]\,\underbrace{[\phi][G]}_{[\phi_{\text{def}}]} = [G^\top][Q_{HH}(ik)][G] \tag{8}$$

where $[AIC(ik)]$ is the discrete aerodynamic influence coefficient matrix of the undeformed wing, assumed to be unknown explicitly and unchanged due to the deformation, and $[Q_{HH}(ik)] = [\phi]^\top[AIC][\phi]$ is the generalized aerodynamic coefficient matrix. Unlike the `SHARPy` formulation that evaluates the aerodynamic model at each deformation, in the current MRM formulation the aerodynamic model is only evaluated once. The aerodynamic forces rotate and move with the deformation, but the AIC matrix is assumed constant. This increases computational efficiency but may lead to inaccuracies at larger deformations as will be shown in the results section. Given the deformed, linearized stiffness, mass, and aerodynamic matrices about a static equilibrium at prescribed flow conditions, flutter can be evaluated with any frequency-domain flutter solution technique, such as the k-method used in the current study.

III. Case Study: Pazy Wing

The Pazy wing [29] is a highly flexible wing which has been recently designed for wind tunnel aeroelastic experiments to serve as a benchmark for flexible wing studies. A diagram is provided in Fig. 3a; it has a chord length of 100 mm, a span of 550 mm, and a NACA 0018 airfoil rib profile. The wing structure is made of an Aluminum 7075 spar, of

dimensions 550 mm (length) by 60 mm (width) by 2.25 mm (thickness), and a Nylon PA2200, 3D-printed, chassis. The wing is covered with Oralight foil, a polyester which is typically used in radio-controlled drones. A 300 mm long and 10 mm diameter wing-tip rod is 3D printed as part of the chassis. The rod is used for attaching weights (via drilled holes) that can modify the dynamic properties of the structure and alter the flutter speed. Overall, the wing weighs 0.32 kg (wing tip rod included) without the base with which it attaches to the wind tunnel floor. The built-up experimental specimen is shown in Fig. 3b.

The build of the Pazy wing model analyzed computationally in this paper is referred to as Pre-Pazy Wing Model. This first prototype was used in the experimental static tests which will be referred to herein. A similar experimental model, with minimal modifications (mainly due to manufacturing and to enable new measurement devices), has subsequently been built and tested in the wind tunnel [29]. However, the differences between the two models are sufficiently small such that the use of the Pre-Pazy wing model was deemed acceptable to assess the aeroelastic characteristics in preparation of the flutter experimental campaign.

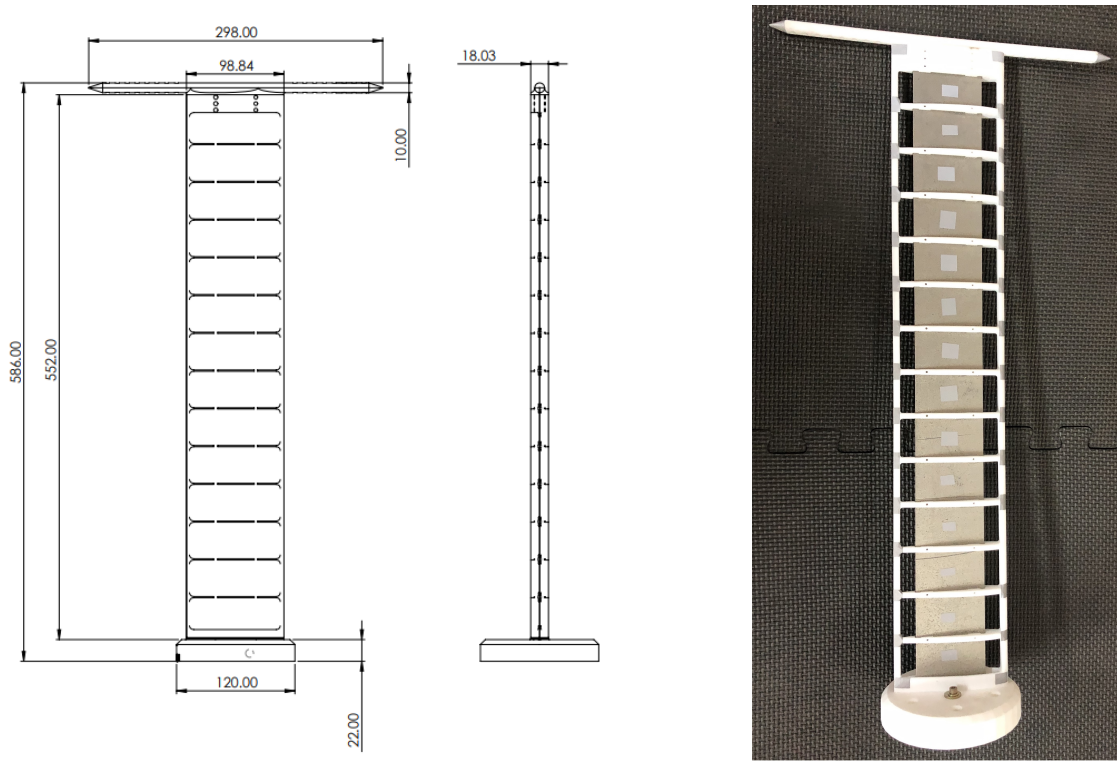

(a) Pazy wing schematic diagram **(b) Pazy wing experimental model.**

Fig. 3 Pazy wing dimensions and experimental model

A. Finite Element Model

The Pre-Pazy wing has been modeled in Solidworks and analyzed using MSC Nastran. The finite element model is shown in Figure 4. Two different models were constructed: one without the skin and one with the skin. In addition, two

subsequent models that also include an additional 10 g mass 40 mm downstream from the wingtip have been used to explore its effect on flutter in the zero angle of attack case (see Sec. V.B). The models have been fine-tuned against ground vibration test measurements as described in Ref. [29]. However, these are assumed straight and do not include a small initial bending curvature present in the manufactured wing.

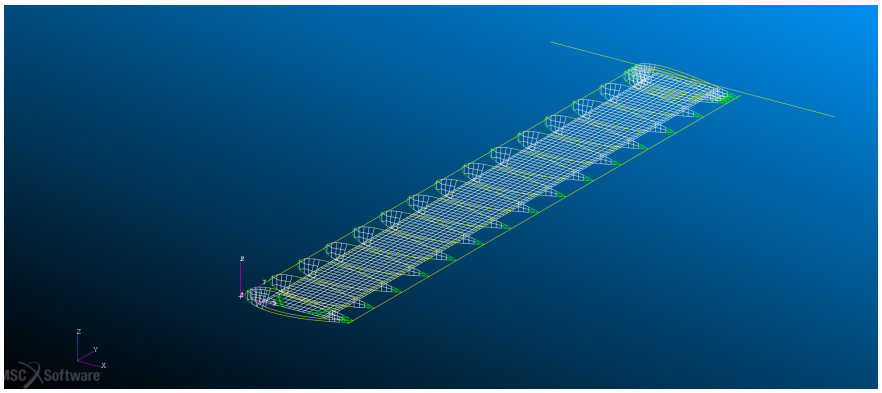

Fig. 4 Finite-element model (skin off).

B. Model Reduction

`SHARPy`'s structural module uses one-dimensional beams, whose sectional properties are defined by 6-by-6 stiffness and mass matrices. To obtain these, the 3D FEM can be loaded in several directions to find the associated equivalent beam stiffness coefficients, whereas the inertial properties at the beam nodes can be derived from the FE model's full lumped mass matrix. Ref. [46] describes the development of the equivalent beam model for its use in UM/NAST (University of Michigan Nonlinear Aeroelastic Simulation Toolbox) using their Enhanced FEM2Stick (EF2S) framework. UM/NAST employs 4-by-4 equivalent sectional stiffness and mass matrices are obtained along a beam reference line (located at 44.1% chord). The difference in the stiffness matrices between UM/NAST and `SHARPy` lies in the shear terms included only in the latter, which have been modeled with infinite stiffness with no impact on the modal characteristics of the beam.

No structural damping has been modeled, which can significantly modify the post-flutter characteristics limiting the amplitude of oscillations of a divergent flutter mode to stabilize them into an LCO. In the case of very flexible wings, damping may change with large deformations. LCOs may be initiated by classical flutter mechanisms but the reasons for their bounded amplitude may be less clear [17]. This was observed in [18], where the use of nonlinear damping profiles as a function of response amplitude successfully managed to numerically replicate in-flight observations of LCOs. These profiles were verified later experimentally [19]. Other ways to introduce damping models can be found in [47–49].

The Pazy wing's Nylon ribs have a NACA0018 airfoil shape which is symmetric, therefore modeled as a flat plate of vortex panels in `SHARPy`. For static simulations, the wake is modeled by infinitely long horseshoe vortices whereas,

for dynamic ones, the circulation shed by the bound vortices is convected downstream from the deformed wing and retained, resulting in a wake sheet of discrete vortex panels of constant circulation that keep a history of the aerodynamic unsteady effects. The aerodynamics of the *skin-on* and *skin-off* models are identical.

For consistency between the baseline models, the MRM structural model was based on a coupled 6-by-6 beam model built in Matlab with the stiffness coefficients from [46] and, like in `SHARPy`, infinitely rigid shear terms. Twenty mode shapes were extracted from 100 FE nodes along the beam and interpolated to 400 segments along the reference line over the wingspan. A similar analysis based directly on the FE model without the beam reduction can be found in [44].

The MRM aerodynamic model is based on the doublet-lattice method. A rigid analysis of the undeformed wing was conducted in ZAERO [50]. For the static aeroelastic analysis, the integrated forces per strip were used to generate a strip model, with the aerodynamic normal force coefficient slope and center of pressure location varying along the span as shown in Fig. 5. The generalized aerodynamic coefficient matrices of the undeformed structure, $[Q_{hh}]$, were obtained in ZAERO at several reduced frequencies and used as a database for the flutter analysis of the deformed wing.

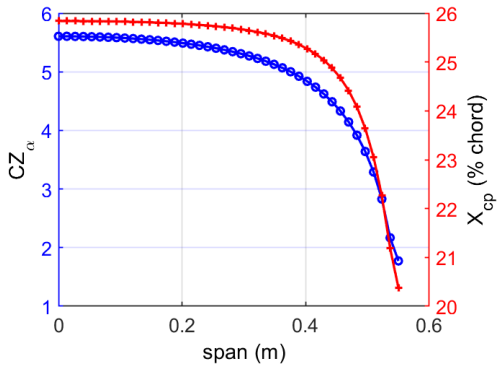

Fig. 5 Spanwise distribution of the sectional normal force coefficient slope and center of pressure locations, computed from ZAERO for the undeformed structure and used in the MRM model.

C. Modal Analysis

A modal analysis of the unloaded Pre-Pazy wing has been performed to validate the sectional coefficients of the equivalent beam models against the full 3D FEM in which the frequencies are compared. Tables 1 and 2 show the original FEM, UM/NAST [46], `SHARPy` and MRM frequencies. Since the `SHARPy` and MRM models are derived from the UM/NAST model it is this data that we use to compare our models against. For a performance evaluation of the one-dimensional beam model compared to the full 3D FEM the reader is referred to [46], although the good agreement between the full 3D FEM and the one-dimensional beam model justifies its use. Turning to the models used herein, the `SHARPy` and MRM models, with maximum errors of 0.7% against the UM/NAST model in the 3rd out-of-plane (OOP3) bending mode can be considered acceptable.

Table 1 Modal frequencies comparison with the skin fitted.

Mode		NASTRAN [Hz]	UM/NAST [Hz]	SHARPy [Hz]	MRM [Hz]
1st OOP bending	OOP1	4.67	4.68	4.69	4.67
2nd OOP bending	OOP2	30.68	30.82	30.87	30.69
1st torsion	T1	43.57	43.51	43.71	43.40
3rd OOP bending	OOP3	87.97	88.82	88.19	87.64

Table 2 Modal frequencies comparison without the skin.

Mode		NASTRAN [Hz]	UM/NAST [Hz]	SHARPy [Hz]	MRM [Hz]
1st OOP bending	OOP1	4.42	4.42	4.43	4.41
2nd OOP bending	OOP2	29.02	29.11	29.15	28.99
1st torsion	T1	41.53	41.44	41.63	41.34
3rd OOP bending	OOP3	83.34	83.92	83.34	82.78

IV. Static Results

The static tests performed include structural-only simulations and steady aeroelastic simulations and are used to compare SHARPy and the MRM models. The experimental results shown for both the structural tests and the wind tunnel tests have been obtained from Ref. [51] and Ref. [29]. In the comparison against the experimental data, it must be noted that the manufactured Pre-Pazy wing had a slight initial curvature which had a small effect on the structural tests (Sec. IV.A and Sec. IV.B), yet it has not been accounted for in the one-dimensional beam reduction process [46], and thus in the SHARPy model. The MRM models included this initial curvature by using a bent reference line, however, the modes employed in the MRM method are those of the straight wing configuration. The justification for the use of the undeformed mode shapes is that the small changes in the initial geometry (approximately 4% span) have a small effect on the linearized system's modal properties, as will be shown in Sec. V.A (Fig. 10).

A. Bending structural tests

Static bending tests have been performed to compare the stiffness properties of the equivalent beam models to experimental results [51] and to explore the effect of the different modeling features across SHARPy and the MRM; namely the use of the undeformed geometry versus including the initial deformation on the reference line only (as the modes are those of the straight wing configuration). Therefore, we will refer to these numerical results by the modeling features rather than the code used to derive them.

The bending test is performed by placing a dead load at the wing tip at the mid-chord position, which is also the station at which deflection is measured. Numerical results obtained using the undeformed model (SHARPy) and that including the jig shape deformation (MRM) are compared to the experimental data set in Fig. 6. The initial set-up for the experimental procedure differed for this test between the *skin on* and *skin off* specimens, where the former was set-up with the initial curvature facing upwards and the latter facing downwards and this changed the bending stiffness,

in particular at large deflections.

First, to visually aid the comparison between models and observe the effect of the initial curvature on the gradient and nonlinear behavior, the offset in the initial deformation has been removed from Fig. 6 and, in turn, it is tabulated in Tab. 3.

In the *skin on* case in Fig. 6a, it can be observed how the nonlinear geometrical stiffening appears first on the model not including the deformation. This is as expected since, it being a geometrical effect, installing the wing with its curvature opposing its self-weight introduces a delay in these effects appearing. In terms of the gradient on the linear part of the curve, the undeformed model presents a 5% stiffer response.

Turning to the *skin off* case in Fig. 6b, the difference in gradient between the computational models is not as apparent, yet there is an 8% difference with the experimental dataset's gradient. In addition, the differences in the nonlinear behavior are significantly less obvious than in the previous case. However, the stiffening does appear under a lighter load in the deformed curvature case, since it is now that one that starts with a larger zero-load deformation. The experimental results show greater compliance than the deformed curvature model, although this could be due to experimental uncertainty in the measurements which is not available.

The effect of the skin in increasing the stiffness is clear from the gradient and zero-load deflections in Tab. 3. From the undeformed model we can extract that the skin increases the stiffness by approximately 11%. Regarding the inclusion of the deformed geometry on the beam reference line, given the $\approx 5\%$ difference in the gradient of the linear part in the most different condition (*skin on* test), we have the confidence in that neglecting the initial zero-load deformation will not negatively impact subsequent analyses, and will make the model simpler for others to use.

The data series shown in Fig. 6 are available in the supplemental materials in the folder `01_Bending`.

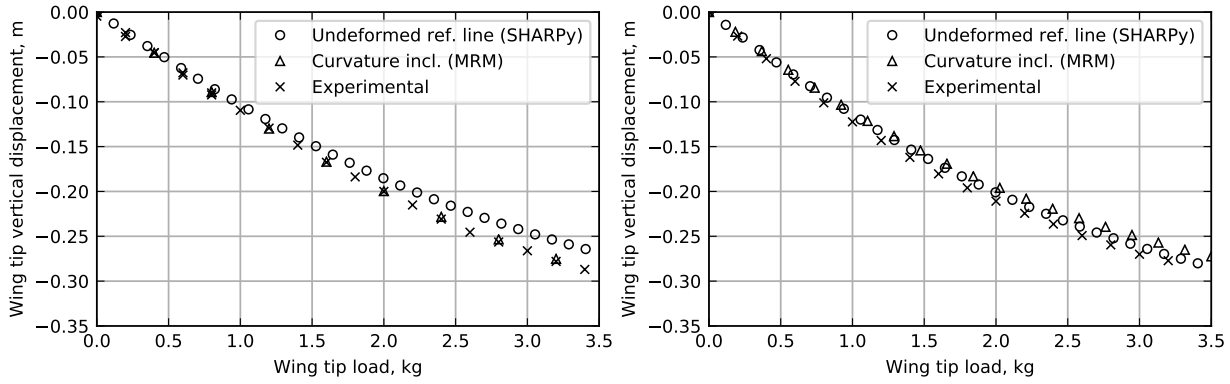

(a) Skin on **(b) Skin off**

Fig. 6 Wing tip, mid-chord vertical displacement comparison under a dead load between undeformed reference line model (`SHARPy`), the model with initial curvature included (MRM) and experimental results.

Table 3 Linear bending curve slope for a linear regression coefficient of 0.999 for the bending test up to 1 kg load and static deflection under self-weight for a static deflection bending test under self-weight and 1 kg tip load at the center of the wingtip chord.

	With skin		Without skin	
	Gradient [cm/kg]	Static deflection [cm]	Gradient [cm/kg]	Static deflection [cm]
Straight ref. line (`SHARPy`)	-10.43	-1.57	-11.57	-1.79
Initial curvature incl. (MRM)	-11.14	0.83	-11.46	-3.72
Experiment	-11.09	0.89	-12.64	-4.04

B. Torsional structural tests

Torsional tests were performed on the manufactured wing [51] and compared to the numerical results. This test involved a dead weight being placed at the wing tip, 80 mm ahead of the leading edge. Note that the wing tip rod, shown in Fig. 3b, to which the load is attached is modeled as a rigid member. In this test, both the *skin on* and *skin off* experimental set-ups had the specimens installed with the initial curvature facing upwards. Figure 7 shows the wing tip, mid-chord vertical displacements for all models, which are in good agreement, with the static offsets removed as explained in Sec. IV.A. Figure 8 shows the wing tip twist angle, θ_{tip}, which was approximated as

$$\theta_{\text{tip}} = \arctan\left(\frac{z^{\text{LE}} - z^{\text{TE}}}{x^{\text{LE}} - x^{\text{TE}}}\right), \tag{9}$$

where z and x refer to the vertical and horizontal coordinates of the deformed wing, respectively, measured in an inertial frame with y along the span of the undeformed wing. LE and TE denote the leading and trailing edges, respectively. The response shown by both numerical models is consistent with that explained in Sec. IV.A accounting for by the initial jig deformation. In addition, the comparison to the experimental data set is again good, considering that the twist angle as computed by (9) involves measuring several displacements and the subtractions involved propagate the uncertainty. The shift observed in the experimental data set beyond the 1.0 kg load in Fig. 8b is attributed to a measurement error. However, the gradient of the curve up to the 1.0 kg point is in good agreement between the undeformed reference line (`SHARPy`), including the curvature in the reference line (MRM) and the experimental data set.

The results shown in Fig. 7 and Fig. 8 are provided in the Supplemental Materials in folder `02_Torsion`.

C. Steady aeroelastic simulations

This simulation replicates a wind tunnel test in which the wing is clamped vertically at a set angle of attack and placed in a steady, uniform flow. The wing is fixed to the wind tunnel floor by means of a round base attachment (see Ref. [29, Fig. 18b]) which is rigid and the wing aluminum spar is bolted to it such that there are no deflections inboard of the span zero location. Aerodynamically, the round base does not generate lift and, even though it may have an effect, it is

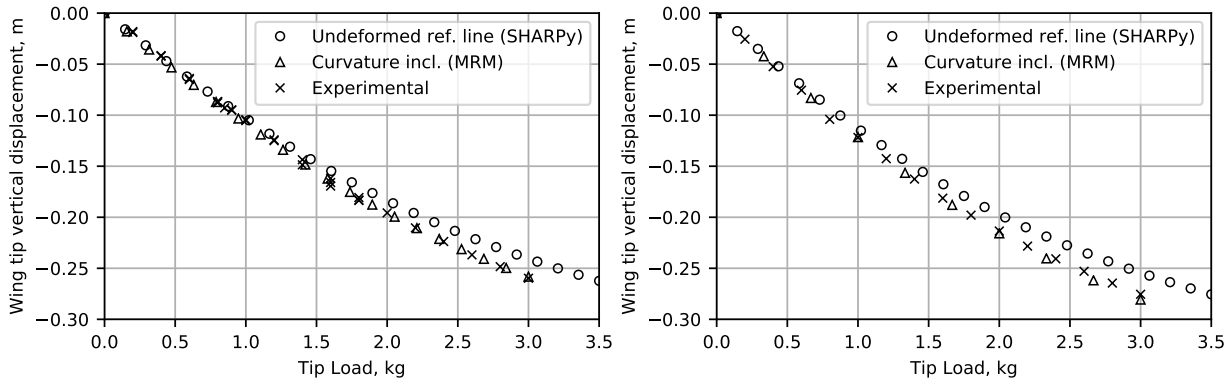

(a) Skin on **(b) Skin off**

Fig. 7 Wing tip, mid-chord vertical displacement comparison under a twisting dead load between SHARPy, MRM and experimental results.

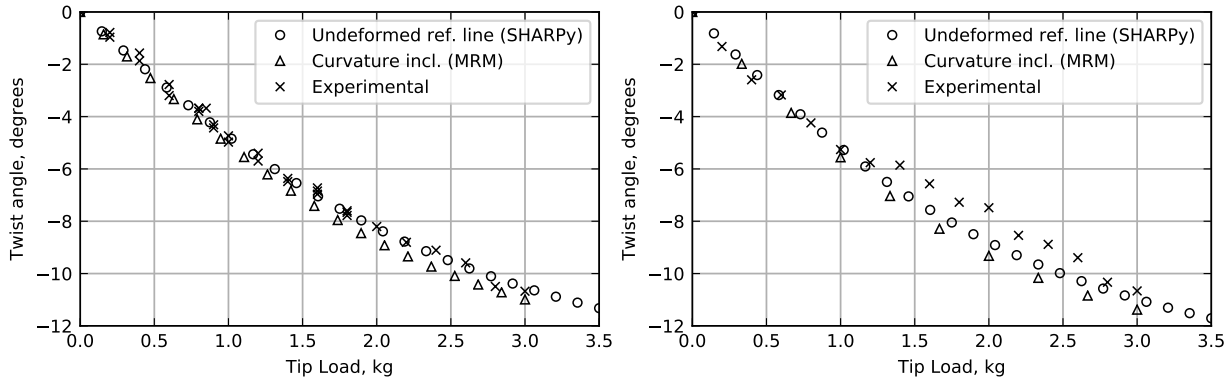

(a) Skin on **(b) Skin off**

Fig. 8 Wing tip twist angle under a tip load (negative twist indicates leading edge down).

likely small and cannot be included in our current aerodynamic models. In addition, no correction has been applied to include wind tunnel wall effects since the distance of the specimen to the walls is considered sufficient to neglect these. Following from the results of the structural tests, the numerical models use a straight reference line given the small effect of the initial curvature; thus, in terms of structural properties the SHARPy and MRM beam models are equivalent and we refer to them by the code name rather than modeling features.

The results obtained from SHARPy use the nonlinear structural solver and UVLM with an infinite horseshoe wake (which deforms with the wing) with symmetry boundary conditions at the wing root (base of the spar) simulating the wind tunnel floor. The MRM uses the aerodynamic model of the rigid (undeformed) wing configuration. The wing is tested at several angles of attack and free stream velocities, with full simulation details in Table 4, and compared to the wind tunnel tests.

Figure 9 shows the wing tip out-of-plane displacements at the midchord expressed in an inertial frame of reference

Table 4 Steady aeroelastic simulation conditions and SHARPy/ZAERO panel discretization.

Angle of attack	5°, 7°
Free stream velocity	$1 - 60\,\mathrm{m/s}$
Density	$1.225\,\mathrm{kg/m^3}$
Chordwise panels	16 (SHARPy), 20 (ZAERO)
Spanwise panels	32 (SHARPy), 40 (ZAERO)
Wake panels	Infinite horseshoe (SHARPy)

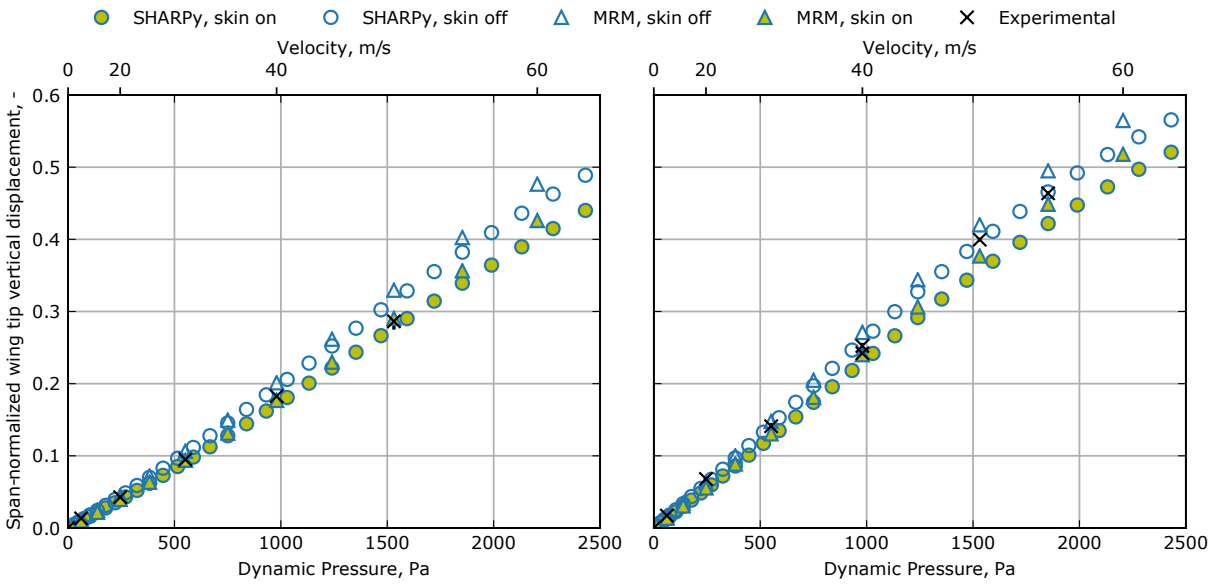

(a) 5 degrees **(b) 7 degrees**

Fig. 9 Wing tip out-of-plane deflections at various angles of attack and free-stream velocities.

with origin at the wing root and aligned with the flow (the structure rotates to simulate the angle of attack). Numerical results are shown for both *skin on* and *skin off* models in order to show the uncertainty in the stiffness introduced by modeling the Oralight skin present in the wind tunnel test specimen. The displacement shows a linear relationship with dynamic pressure below 1000 Pa (40.4 m/s) and in this region the results from all computational models and the experimental results are in good agreement. At the higher velocities, once deflections increase beyond 30%, the dihedral effect in the aerodynamics becomes the major difference between SHARPy and the MRM, although its effect is small as the MRM displays just a slightly more compliant response, with the displacement approximately 5% above that of SHARPy at 60 m/s. The general trend gives confidence in the validation of the static aeroelastic model paving the way to the dynamic results, which are presented next. In addition, the experimental results fall within the *skin on* and *skin off* numerical predictions, showing that the use of these two models is adequate to gauge the contribution to the wing stiffness of the Oralight skin. Finally, the results support not modeling the wind tunnel floor attachment and neglecting any blockage effects. All results in Fig. 9 are contained in the Supplemental Materials `03_StaticAeroelastic` folder.

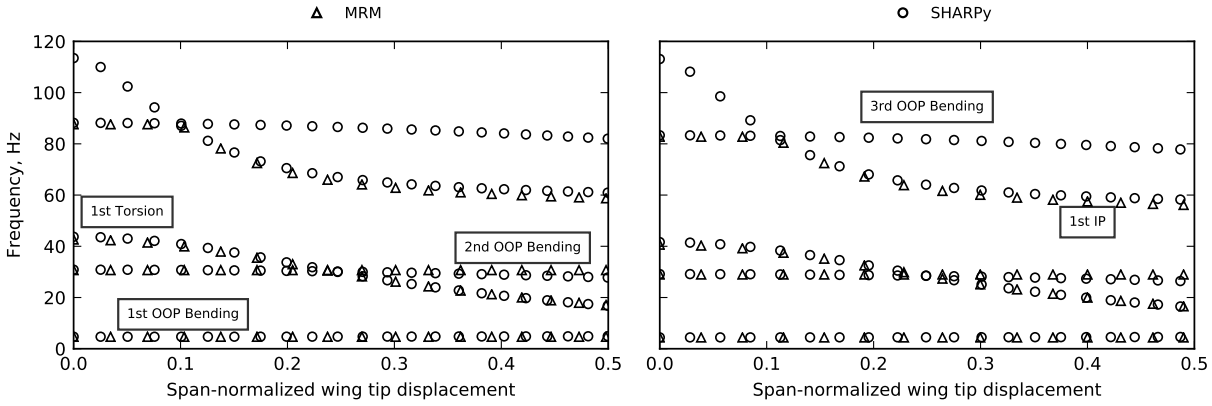

(a) Skin on **(b) Skin off**

Fig. 10 Linearized beam's modes of vibration frequencies at a deformed condition when subject to a wing tip vertical follower force.

V. Dynamic Results

The previous results show good agreement between SHARPy, the MRM and the experimental results for static cases. To verify the inertia properties of the model, we will compare the vibration modes of the deformed wing under a follower force using the computer models only*. Then, we proceed with a flutter prediction analysis for the wing in the wind tunnel fixed in a vertical position at various angles of attack to evaluate the variation in flutter speed. In addition, for the zero angle of attack case only, we also test the effect of a 10 g mass at the trailing edge of the wing tip section to evaluate its impact. This mass is modeled as a lumped point mass with no inertia.

A. Deformed wing modal analysis

A modal analysis is performed on the deformed Pazy wing by placing a vertical follower force at the wing tip node (located on the beam reference line at 44.1% of the chord). This illustrates the change in the natural modes of vibration of the structure as the wing deforms, which will have a significant impact on the flutter mechanics, as will be seen in the next subsection. The applied follower force at the wing tip node is aligned with the local vertical axis, therefore, in the linearization of the structural system there are stiffening terms that arise due to the dependency of this force on perturbations to the structural degrees of freedom (by means of changes to the frame of reference on which it is defined) [34].

Figure 10 compares the deformed structural frequencies between SHARPy and the MRM for both the *skin on* and *skin off* cases. The structural change of shape, in this case parametrized by the vertical wing tip deformation, causes two clear mode switches. Of particular importance is the drop in frequency of the 1st torsional mode, which crosses the 2nd out-of-plane bending mode at approximately 25% spanwise deformation, and the drop in frequency of the 1st in-plane

*In some cases it is possible to measure those as was done in Ref. [28] however in the Pazy wing such a methodology was not possible because the deflection under self weight was too small to affect the frequencies

mode. The out-of-plane bending modes remain fairly constant in frequency, with the OOP1 seeing a slight increase in frequency caused by the stiffening terms arising from the linearization of the wing tip follower force. We note that these results are only indicative as aerodynamic loading produces different equilibrium shapes than these and thus would skew the frequency versus wing tip displacement relation. These results are provided in the Supplemental Materials `04_DeformedModal` folder.

B. Zero angle of attack wing flutter prediction

At zero degree angle of attack, there is no structural deformation with increasing wind speed. Therefore, the flutter boundary of the wing can be predicted using a conventional linear analysis software like NASTRAN. In `SHARPy` the aeroelastic system is linearized around the straight wing shape (zero deformation) to simulate the vertical mount on the wind tunnel. The linear UVLM and structural models at this condition are obtained as detailed in Sec. II.A. The UVLM is non-dimensionalized with respect to the free-stream flow, making it independent of velocity [41] while translating that dependency in velocity into a time scaling in the structural model. Consequently, a single aerodynamic model can be built which is valid across all incompressible flight velocities (as in the doublet-lattice method). It is then coupled to a structural model that needs updating at each wind speed condition through its mass and stiffness matrices, that had been scaled with the reference time (dependent on the free stream velocity) as updating the structural model at every wind speed is significantly more efficient than updating the linear UVLM. This is due to the required discretization to achieve convergence which leads to UVLM systems of 10^5 states, compared to the structural system's dimension, which is twice number of structural modes retained, in this case only six modes.

However, as explained in Sec. II, the linear UVLM system is reduced using a Krylov sub-space method, which matches the steady state gain of the system's transfer functions. The resulting aeroelastic state-space model is small (42 states: 30 aerodynamic and 12 structural — corresponding to 6 modes —), and can be quickly evaluated for the desired wind speeds. The stability analysis is performed by computing the eigenvalues of the system, shown in Fig. 11b, between 10 and 100 m/s at a density of $1.225\,\mathrm{kg/m^3}$. Fig. 11a shows the corresponding V-g plot with the calculated frequency and damping at each velocity. In `SHARPy`, the wing is discretized with 16 chordwise panels, 32 spanwise panels (16 3-noded finite element beams) and a 16-chord wake.

The MRM undeformed flutter prediction is based on a k method analysis that uses the modal structural properties and the generalized aerodynamic matrices obtained from ZAERO. Results have been verified against a g method analysis conducted internally in ZAERO [50, 52, 53]. The highest k value in the current MRM analysis is 1.5, which is sufficiently high considering the flutter reduced frequencies, which are lower than 0.1. The plot results will be presented for a minimal velocity of 20 m/s and 43 Hz, which corresponds to a k value of approximately 0.6.

For the results presented in this and subsequent sections, the denoted damping ratio corresponds to viscous damping, ζ, where for an eigenvalue of the system given by $\lambda = \sigma \pm j\omega_d$, the natural frequency is $\omega_n = \sqrt{\sigma^2 + \omega_d^2}$ and the

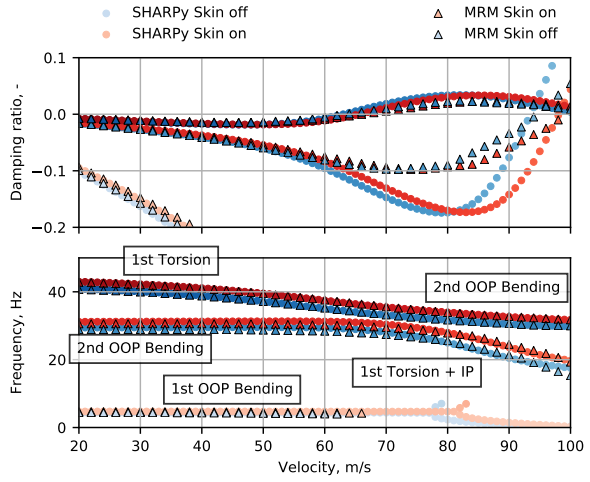

(a) Frequency-damping, with modes colored according to natural frequency.

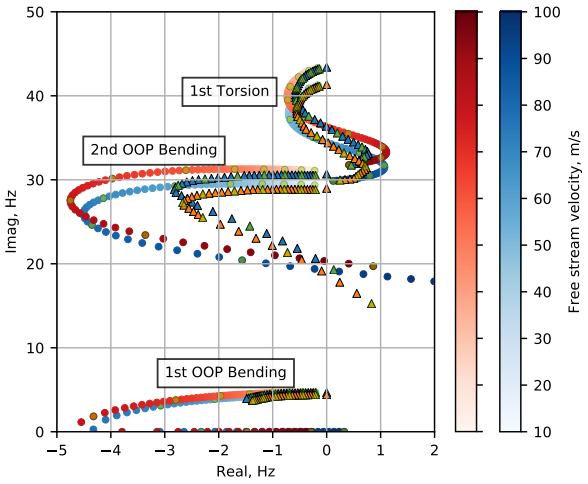

(b) Eigenvalues, highlighted (in green) at 10 m/s intervals.

Fig. 11 Stability diagrams of the reference configuration at zero angle of attack.

damping ratio $\zeta = \sigma/\omega_n$, thus a positive value for ζ indicates an unstable system. Damping values obtained from the g-method used by the MRM are converted to the viscous damping convention as $g \approx 2\zeta$. Due to relatively low structural damping that was measured in the GVT (about 0.2%) in the current work the structural damping was not examined. However, its effect on the wing flutter was studied separately in [54].

The flutter analysis is performed for both *skin on* and *skin off* models to evaluate the sensitivity to structural properties and, in particular, stiffness. This can be used to estimate the uncertainty in the flutter speed prediction due to inaccuracies in the structural models as the Oralight skin fitted on the wind tunnel specimen is complex to model. The major contribution from the skin appears in the stiffness properties, in particular the out-of-plane bending stiffness which is, on average along the span, 11% larger than in the *skin off* model. Also, due to the linear nature of the constitutive relations of the beam models, the contribution to the stiffness is likely overestimated, as these models are unable to capture the local buckling of the skin on the suction side as soon as the wing deforms. Thus, by comparing these two models (*skin on* vs *skin off*) we obtain a range of results where we expect to find the experimental ones.

The stability analysis for the wing at zero angle of attack in Fig. 11 shows that the increased airspeed causes a reduction in frequency of the torsional mode (T1), whose eigenvalue coincides with the second out-of-plane (OOP2) bending mode and results in the first flutter instability. This occurs both in the *skin on* and *skin off* models at very similar speeds, listed in Table 5, since the added stiffness of the *skin on* case (predominantly in out-of-plane) increases the zero-velocity separation between OOP2 and T1 by just 0.5 Hz (4%), and this translates into a flutter speed increase of 2 m/s (3.1%) between both cases.

Beyond this first instability, the torsional mode continues to drop in frequency, causing the flutter mode to cross

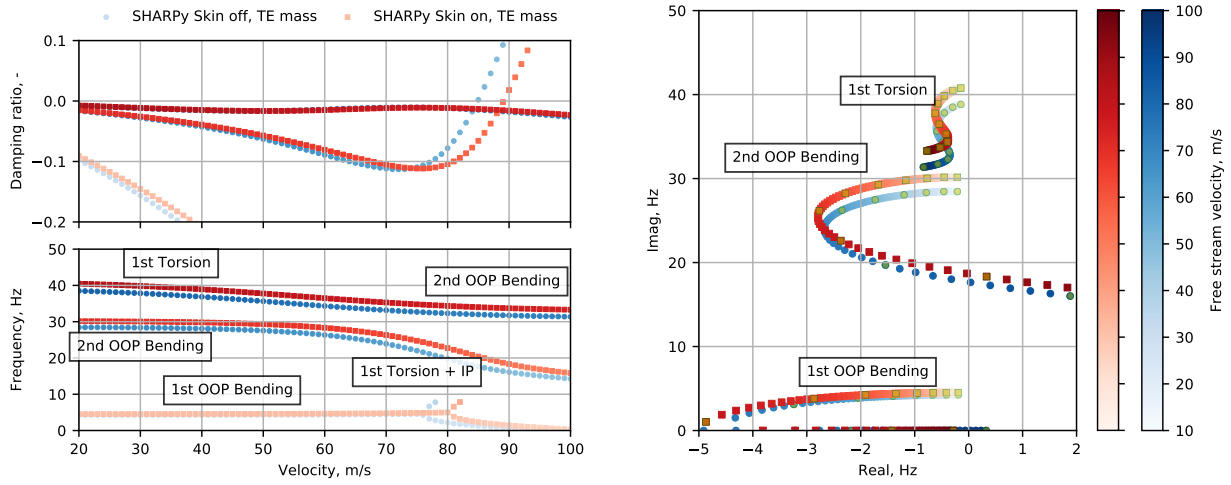

(a) Frequency-damping, with modes colored according to natural frequency.

(b) Eigenvalues. Highlighted (in green) eigenvalues at 10 m/s intervals.

Fig. 12 Stability diagrams at zero angle of attack with a 10 g wingtip trailing-edge mass. Results from SHARPy.

back over to the left-hand plane (the "hump" in Fig. 11). However, prior to the first flutter mode crossing back over the imaginary axes, a second flutter instability has occurred, this time a coupled torsion and first out-of-plane bending mode.

The comparison between SHARPy and the MRM highlights the differences between the eigenvalue analysis of the linearized state-space and the k-method. Although the predicted flutter speed is acceptably similar between the two methods (the relative error between SHARPy and the MRM in the flutter speed is less than 1.6%), at speeds other than flutter, the results also include differences arising from the chosen solution method given that the k-method assumes zero damping, therefore, only approximates the problem when the conditions are different, while the UVLM-based eigenvalues correspond to the actual linearization of the physical system including the damping. An implication of this is that actual occurrence of flutter may be more abrupt that it would be predicted by standard the k-method, which poses an additional challenge on the experimental campaign. Note that although the k-method is frequency-based and typically sampled for constant reduced frequencies, an interpolation has been performed to obtain results at constant velocity intervals. Therefore, the velocity vector associated to each mode is different and, in the case of the OOP1 mode, the MRM results are limited to 65 m/s.

Additionally, for the purposes of the wind tunnel campaign, we explore the effect of including the wingtip mass on the stability properties shown in Fig. 12. With the mass added at the trailing edge of the wing tip, the torsional mode is damped to the point that it does not cross the imaginary axis, hence the first flutter mode (T1-OOP2) is suppressed. However, after T1 switches with OOP2, it does not go as far into the left-hand plane in Fig. 12b as compared to the nominal case. Therefore, the effect of the trailing edge mass is to significantly increase the flutter speed of the wing by suppressing the first unstable mode, thus considerably delaying the onset of the second flutter mode, as seen in Table 5.

To sum up, for the straight wing flutter in the nominal condition, Table 5 outlines the flutter speed at zero degrees obtained using SHARPy and compared against the results from ZAERO coupled with the MRM* showing good agreement. Note that the flutter instability with the trailing edge mass attached corresponds to a first bending and first torsion flutter mode, as opposed to the nominal case in which flutter is a first torsion with second out-of-plane bending mode.

Table 5 Predicted flutter speed of the wing at zero angle of attack.

	Nominal	Trailing edge mass
SHARPy with skin	65.0 m/s	89.1 m/s
SHARPy without skin	63.0 m/s	84.0 m/s
ZAERO / MRM with skin	66.1 m/s	89.4 m/s
ZAERO / MRM without skin	63.4 m/s	85.2 m/s

These results may be found in the Supplemental Materials `05_StraightWingFlutter` folder.

C. Flutter prediction for the deformed wing

Predicting the flutter speed for the deformed wing configuration is a more complex problem given that at the new reference point the steady forces at non-zero angles of attack may impact the stability of the wing [3] and the large deformation changes the structural dynamics. This was clearly shown in Fig. 9 where, for example, the deflection of the wing set at 5 degrees angle of attack changes from 10% to 30% of span between 30 and 50 m/s causing the dynamics of the structure to change significantly, with the first torsional mode at approximately 25 Hz as opposed to the in-vacuo, undeformed 42 Hz, shown in Fig. 10.

Therefore, computing the flutter speed of the deformed wing becomes an iterative procedure. In SHARPy, the system is first linearized around an initial guess value for the flutter speed and the flutter speed is estimated using the linear system as described in the previous section. Then, the nonlinear equilibrium condition at this computed flutter speed is found, the system linearized and the flutter speed estimated again. This fixed-point iteration continues until the flutter speed estimation using linear methods converges to the speed at which that system was linearized and its nonlinear shape computed, which has been found to converge in 5-10 iterations for the Pazy wing cases. We will refer to this point as the matched flutter point as this process is analogous to the iterations on Mach number used in subsonic aeroelastic analyses. This approach is the most efficient should the flutter speed be the objective metric to be found. However, the dynamics at points other than the flutter speed are also of interest in order to produce velocity-frequency-damping data across the envelope. Therefore, the parameter space was sampled in 1 m/s speed increments and at each point the system linearized and the eigenvalues found, thus producing the damping data which will show the onset and offset of instability. The flutter prediction has been under the same conditions as those in the previous section.

In the case of the MRM, a non-matched k-method flutter solution was conducted on the system, linearized about

*In an undeformed case, the MRM simplifies to a k-method analysis with ZAERO based aerodynamic matrices and is equivalent to ZAERO flutter analysis.

a statically deformed shape, at prescribed flow conditions (angle of attack and free stream velocity). The matched solution is obtained by interpolating the results of the k-method to the prescribed velocity at which the equilibrium was evaluated. By doing this at increasing prescribed velocities a matched $V-g$ plot can be obtained. Alternatively, if only the flutter velocity is of interest, the iterative fixed point iteration procedure described in the previous paragraph can be used. The analysis used the fully modal MRM approach, in which the solution is based only on modal (generalized) inertial and aerodynamic matrices, without the need for an explicit (discrete) representation of the two [44].

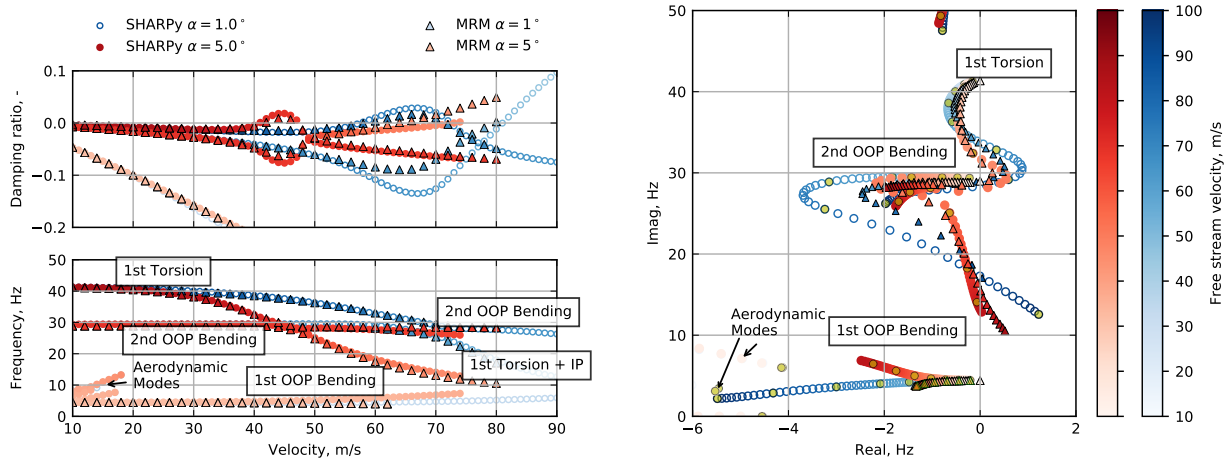

(a) Frequency-damping, with modes colored according to natural frequency.

(b) Eigenvalues, highlighted at 10 m/s increments.

Fig. 13 Stability diagrams for the skin-off wing at 1 and 5 degrees angle of attack.

The effect of large deformations on flutter can be illustrated by means of stability plots obtained for two values of the root angle of attack (1 and 5 degrees) in Fig. 13 and 14 for the *skin-off* and *skin-on* models, respectively. Both wing models are considered to have a plausible flutter boundary given the uncertainty introduced through the modeling of the Oralight skin.

The first effect that the angle of attack, and thus increased deformation, has on stability is to decrease the flutter speed. At higher angles of attack, the torsional mode observes a much steeper drop in natural frequency which advances the coalescence with the second out-of-plane bending mode. In addition, the cross-over of the two modes occurs at a lower speed and the first unstable flutter region is much shorter, as shown by the narrowing "hump" in the positive damping ratio region. Contrarily to the case at zero angle of attack, this shortening of the hump caused by the wing deformation results in a region of stability beyond the first flutter speed. Note also that the second flutter mechanism follows a similar trend: the increased deformation due to a larger angle of attack brings forward the coalescence of the torsional and first out-of-plane bending modes and therefore reduces the flutter velocity.

We must highlight that the numerical stability analysis in this work is solely based on linear theory, therefore, once an eigenvalue crosses the imaginary axis (damping ratio larger than zero), a divergent flutter mechanism would be

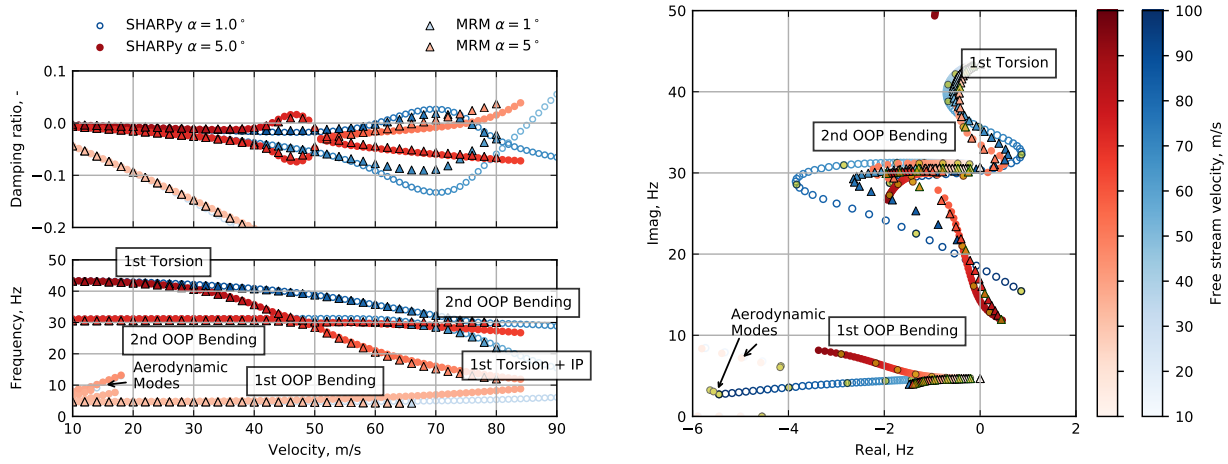

(a) Frequency-damping, with modes colored according to natural frequency.

(b) Eigenvalues, highlighted at 10 m/s increments.

Fig. 14 Stability diagrams for the wing with the skin fitted at 1 and 5 degrees angle of attack.

predicted, where infinitesimal perturbations would grow unbounded. Nonlinear effects (like geometrical stiffening, added internal damping or dynamic stall) may appear once deformations acquire a significant magnitude, which are not captured, and may result in the oscillations remaining fixed in amplitude settling in a stable limit cycle oscillation (LCO). For very flexible wings, like the Pazy wing, it may well be the case that the wing is able to twist and deform until limited by aerodynamic stall, preventing a destructive flutter [23]. In addition, "hump" modes, and in particular those involving OOP2, are more susceptible of being LCOs rather than flutter. In this section, dealing only with linear results, it is cautious to refer to these instabilities as flutter; in the following section detailing the experimental results, LCOs will be readdressed.

Figure 15 summarizes the effects of deformation and free stream velocity by showing the unstable flutter regions, one for each flutter mechanism, and the lines of constant root angle of attack show the wing deformation as the airspeed increases. It can be seen how increasing the root angle of attack brings forward the first flutter mechanism, albeit also making the region on instability considerably smaller (i.e. narrowing the "hump"). This is because at higher angles of attack, a smaller increase in velocity is required to increase the deflection such that the aeroelastic torsional mode crosses towards the left-hand plane of the imaginary axis. This is illustrated by the steep "stabilization boundary" of the first flutter mode, which is fairly constant around 25% wing tip spanwise deformation. Note that at sufficiently low airspeeds, the lower bound of the first flutter unstable region would be set by a (static) stall line which, since the aerodynamic models of choice do not model, has not been included. The effect of aerodynamic nonlinearities at high angle of attack on the flutter characteristics of a very flexible wing have been explored in [22, 23].

The onset speed of the second flutter mechanism is also initially seen to decrease with increased deflection and angle of attack. The reduction in onset speed with angle of attack is not monotonic and, beyond 5 degrees angle of attack, the

SHARPy prediction shows a slight increase in the flutter speed with angle of attack. The stability envelope for the *skin off* model provides the most conservative flutter scenario for a wind tunnel test and, as will be shown in Sec. V.D, can be used for the design of experiments to reach the second flutter instability region without excessive deflections and spending minimal time in the first flutter region. In general, the effect the skin has in these models (assuming linear elastic properties and neglecting buckling in the suction side) is to raise the flutter speed prediction by approximately 4% yet, given the uncertainties in the stiffness properties of the *skin on* model, the *skin off* results should be used for wind tunnel tests design.

Having explained the physical processes behind the changes to the flutter boundary as a result of large deflections, we now turn to a comparison between methods as it is in these deformed, dynamic cases where the differences in the calculation method and the aerodynamic models become most apparent. Some differences may be attributed to the use of an aerodynamic grid based on the undeformed wing in the MRM approach. This is observed in Fig. 15, where the agreement in the flutter boundary is excellent for deformations up to 30% span (the first flutter instability) for the *skin off* and *skin on* conditions, as opposed to the second flutter mode shown which differs substantially at the larger wing tip deflections. In the specific cases shown in Fig. 13a and Fig. 14a, the relative error in the 1st flutter mode speed at 5 degrees ($\approx$ 20% span-wise deflection) is less than 2% for both skin models, compared to the larger error for the second flutter speed that differs by 12% in the 5 degree case (albeit with an $\approx$ 50% span-wise deflection). The differences in the damping of these aeroelastic modes can be attributed to the difference in the solution methods, as explained for the straight wing flutter case in Sec. V.B, as well as the inclusion of the deformed aerodynamic bound and wake vortex lattice in SHARPy. Similarly, the frequency matching is excellent except for the OOP1 mode at high speeds. The mode frequencies are dominated by the deformed geometry of the wing, as seen in the Sec. V.A, which is accurately captured by both methods. However, the differences in the frequency behavior of the OOP1 aeroelastic mode where SHARPy predicts it to increase frequency with velocity in contrast to the MRM prediction where it stays approximately constant, can be attributed to the change of dihedral effect caused by the deformation, which is captured by the linearized SHARPy UVLM but not the MRM implementation of the linearized aerodynamic system, and is most affected by the OOP1 mode shape. Note that by change of dihedral only the aerodynamic solution is considered, since the follower force effect with large deformations is captured by both models. For comparison, in the zero degree angle of attack case in Fig. 11b where there is no deformation, the OOP1 mode approaches the real axis as velocity increases. Once deformation is introduced by means of non-zero angle of attack to the linearized aerodynamic model, the imaginary part of the OOP1 mode actually increases (Fig. 13b and Fig. 14b).

This effect has also been observed in Ref. [42], where the UVLM was also linearized around the straight wing configuration. It was there observed that the frequency of the OOP1 mode decreases with wing deformation when it is obtained using the undeformed wing aerodynamics, while the frequency would increase, as it is observed here, when the linearized aerodynamics are obtained around the deformed equilibrium. In the MRM, as in SHARPy, the linearized

aerodynamic matrices can be updated at each iteration based on a panel model that fits the deformed shape. That, however, would degrade the computational speed and simplicity of the MRM. The most powerful advantage of the MRM framework is that it accurately captures a highly deformed wing's flutter boundary with only the modal data inputs and an aerodynamic database from a single analysis of the straight wing. Additionally, a beam model was used to generate the modal data for the MRM in the current study for consistency with the other frameworks. We note that the MRM does not rely on a model reduction [43], which may require considerable effort and possibly loss of accuracy for complex structural models.

These results are provided in the Supplemental Materials `06_DeformedWingFlutter` folder.

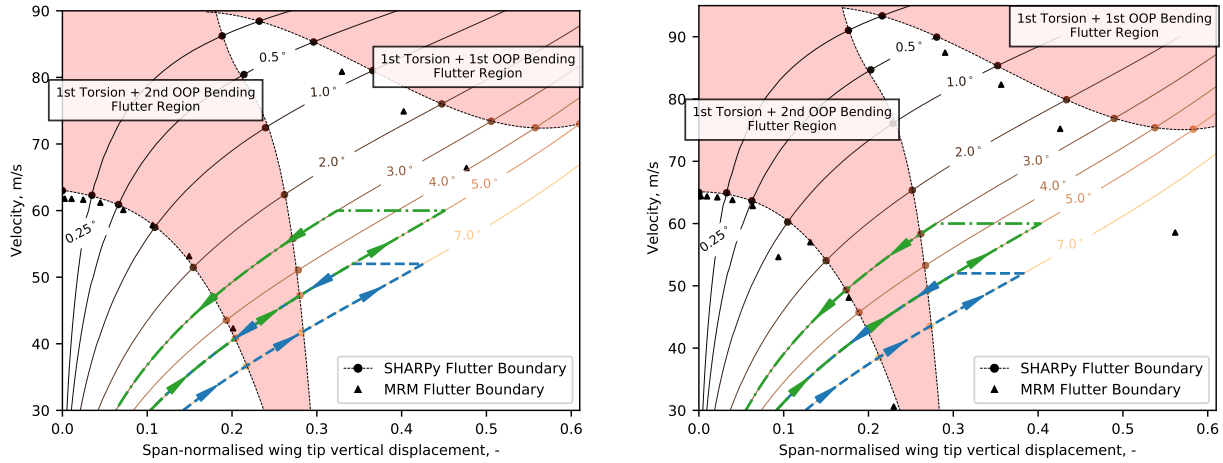

(a) Skin off **(b) Skin on**

Fig. 15 Flutter boundaries and regions, with contour lines showing wing tip deflection at a given root angle of attack. Arrow lines indicate two experimental velocity and angle of attack profiles used in the wind tunnel tests.

D. Comparision with wind tunnel data

The stability envelope presented in the previous section has supported the planning of wind tunnel experiments to explore the first unstable region (T1-OOP2) without incurring excessive airspeeds or deformations. The full test details and results are presented in [55] and only a representative subset of them are used herein to study the capability of the two numerical methods described here to predict the aeroelastic behavior of very flexible wings. This paper, by presenting the Pazy wing, and initial tests of its structural and aeroelastic behavior, will, hopefully, be the foundation for future works that will study the capabilities of the present and other simulation techniques and the physics of this nonlinear system that is rich in experimental, physical, and simulation challenges.

As noted in Sec. III, the wind tunnel test specimen differs slightly from the Pre-Pazy computational model used for this study; however, the small differences between them and the use of *skin on* and *skin off* models in an effort to quantify modeling uncertainty in the Oralight skin make the use of experimental data adequate for our purpose.

Two of the tests in [55] have been used for this work, performing velocity sweeps at several angle of attack values. The tests used are those conducted with angle of attack values between seven and five degrees (airspeed increasing and decreasing, respectively), and between five and three degrees. In each test, the angle of attack was fixed, and the airspeed was continuously increased until wing oscillations started, relying on the wind tunnel natural turbulence to perturb the wing. The airspeed was further increased until the oscillations ceased and the system stabilized. As the wing stabilized at a higher airspeed, the angle of attack was reduced, holding the airspeed fixed. At the new angle of attack, where the wing was still in the stable region, the airspeed was then slowly reduced crossing again through the unstable region until airspeed was reduced to zero. The test angle of attack and velocity trajectories are shown on the stability envelope in Fig. 15; in green for the test between five and three degrees and in blue for the seven to five degrees test. Although the linear analyses are limited to predicting a divergent flutter, the likelihood of the wing entering an LCO as previously described (given it is a "hump" mode with OOP2 contribution and the very flexible nature of the wing) alongside the possibility of exiting the unstable region swiftly by reducing angle of attack or velocity meant that these tests could be conducted with a relatively low risk of structural failure as a result of classical flutter.

Figure 16 shows an example test, starting at 7 degrees angle of attack. Figure 16a shows the airspeed and angle of attack versus time, and Fig. 16b shows the airspeed and strain measured by a Fiber Bragg Grating optical fiber at the front spar, 127 mm from the root. Based on the strain data, at 7.2 degrees angle of attack, with the airspeed increasing, oscillations started at 39 m/s and stopped at 47 m/s, where the onset occurs abruptly and the offset in a more gradual manner. In addition, the amplitude of the strain in the predicted flutter region is relatively constant (and does not show tendency to grow unboundedly), thus indicating that the wing is entering a stable limit cycle oscillation. Similarly, at 5 degrees angle of attack, with the airspeed decreasing, LCO started at 48 m/s and stopped at 36 m/s. This test effectively illustrates the "hump" mode predicted by the numerical models, where for a constant angle of attack the instability is bounded in airspeed.

The onset of LCO, which can be captured by the linear stability boundary, is shown in Tab. 6 for all available tests. They are compared to the predicted lower and upper bounds from our simulations, which have been obtained from the *skin off* and *skin on* models, respectively. It can be seen that despite the slight model mismatch and experimental uncertainty (which has not been accounted for), all test results are within less than 1 m/s from the predicted boundaries.

Despite the models not including any internal structural damping, LCOs may be caused by other source of nonlinearities such as geometrical effects, as would be seen by time marching the aeroelastic nonlinear equations.

Note that the simulations do not capture the LCO offset, that is, the stabilization of the wing as it leaves the unstable region. Capturing this hysteretic behavior in the nonlinear dynamics of the wing needs either time-domain harmonic-balance, or asymptotic analyses, possibly including dynamic stall, which were not carried out in this study. Moreover, while the LCO onset occurs at a distinct airspeed and is straightforward to predict, Fig. 16b shows that the offset occurs gradually over a range of airspeeds, thus indicating that it also depends on the rate of change of the root

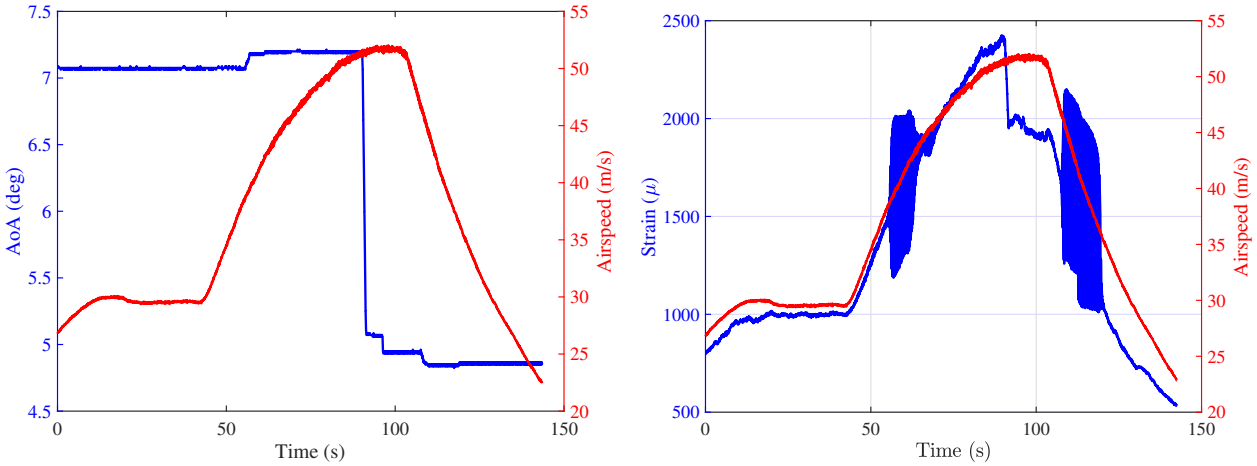

(a) Airspeed and angle of attack settings over time. **(b) Measured strain and airspeed over time.**

Fig. 16 Wind tunnel data for the seven degrees angle of attack test procedure.

Table 6 Predicted and observed onset of instability speed for different angles of attack and airspeed trend.

Angle of Attack [deg]	Airspeed trend	Range of predictions [m/s]	Observed Onset [m/s]
3	Increasing	47.0 - 49.3	49
3	Decreasing	55.8 - 58.4	55
5	Increasing	40.8 - 42.9	43
5	Decreasing	47.3 - 49.3	48
7	Increasing	36.7 - 38.5	39

angle of attack in the test. This behavior is common: where the onset of an LCO matches that of classical flutter, the offset is harder to predict and oscillations usually persist at airspeeds below that at which they started [56].

VI. Conclusions

We have evaluated, compared and validated, using two different nonlinear aeroelastic toolboxes (`SHARPy` and MRM), the structural static and dynamic response of a very flexible wing. The agreement between tools for the different models and correlation with static experimental results have given confidence in using these models to support the planning of wind tunnel experiments to explore the flutter mechanisms of this wing. The two identified flutter modes' dependency on the wing deformation provide an excellent example to showcase the need for nonlinear aeroelastic analysis tools. Both the MRM and `SHARPy` capture well these effects for low-to-moderate wing deformations and accurately predict the first flutter velocity. However, it has been seen how at high deformations corresponding to the second flutter velocity, aerodynamic models linearised on the deformed wing become necessary. These are currently not implemented in the MRM for the sake of simulation speed and minimization of the modeling complexity. However, linear stability analysis tools like the once employed cannot capture nonlinear effects like limit cycle oscillations which, as seen in the experiments, the wing did enter. Although the characteristics of the wing did suggest that the first unstable mode would

actually result in an LCO, this opens the door to further research to include in said stability analysis nonlinear effects, both structural and aerodynamic, for which the Pazy case can serve as validation.

The complex modeling of the Oralight skin introduces some uncertainties into these analyses which, thus far, have been tackled by using two limit cases. By using *skin on* and *skin off* models a flutter speed range is provided that offers insight into the effect of model stiffness uncertainty. Structural damping has been neglected in this study but its effect on the Pazy wing was studied in [44]. Including different damping profiles would modify the flutter predictions and, in particular, post-flutter behavior. The Pazy wing case therefore provides an adequate test bed on which to explore different damping models and the effect on the damping profile of neighboring wing sections rubbing against each other at large deflections, which is proposed as possible further study.

In addition, the wind tunnel test campaign designed using the results in Sec. V produced excellent results in the onset on instability speed comparison, despite the use of a slightly modified test specimen. All experimental instability speeds lie within 1 m/s of the numerically predicted boundary, thus validating the methods with `SHARPy` and the MRM in the prediction of flutter for very flexible wings.

The good correlation between test results and simulation predictions using two alternative aeroelastic simulation capabilities, SHARPy and MRM, demonstrates the capability of these methods to capture by simulation the complex nonlinear aeroelastic behavior of highly flexible wings in the subsonic speed regime. The flutter/LCO mechanisms displayed by the Pazy wing presented here offer interesting insights into the way high deformation of wings affects their aeroelastic behavior. The cases described here invite follow-on research work by others and provide a rich experimental and numerical database for the validation of current and future nonlinear aeroelastic simulation methods. Thus, the models used here and computer scripts have been archived for future use by the aeroelasticity community. More test results are presented in Ref. [55] and new test results of nonlinear aeroelastic systems will be presented in the future.

Research Data

With the objective of making this a benchmark case that can be used to validate and test future aeroelastic simulation tools, the `SHARPy` model, scripts and results are all made available online. The `SHARPy` results have been obtained using version 1.2, which is included alongside the simulation scripts in the repository listed in Table 7. All results presented herein can be downloaded from the Zenodo archive and are made available under the Open Data Commons Open Database License[†]. Any rights in individual contents of the database are licensed under the Database Contents License [‡]. All license details are provided with the results.

The wing model used herein is fully described in [46], where the inertia and stiffness distributions are provided. The `SHARPy` equivalent model is included in the repository listed in Table 7.

[†] `http://opendatacommons.org/licenses/odbl/1.0/`
[‡] `http://opendatacommons.org/licenses/dbcl/1.0/`

Table 7 Online repositories for models, scripts and results.

	URL
AePW3 results database	`https://doi.org/10.5281/zenodo.5560962`
`SHARPy` simulation scripts	`https://doi.org/10.5281/zenodo.5793295`

The repositories in Table 7 are additionally provided with this article as Supplemental Materials, and all the results presented in this work are contained in the `aepw3-results-database` folder and then as specified in the text in the relevant section.

Acknowledgements

The authors would like to gratefully acknowledge the Pazy Foundation for their support of the Pazy-Wing experimental campaign. The authors would also like to thank Dr Markus Ritter from the DLR for leading and coordinating the activities of the Large Deflection working group within the 3rd Aeroelastic Prediction Workshop and Prof Cristina Riso from Georgia Tech for her help providing the UM/NAST model.

Norberto Goizueta would like to thank Mark Korchma from Imperial College for deriving the original equivalent beam model for `SHARPy` that started this work and the Department of Aeronautics at Imperial College for sponsoring his research under EPSRC grant EP/R513052/1.

References

[1] Livne, E., "Aircraft active flutter suppression: State of the art and technology maturation needs," Journal of Aircraft, Vol. 55, No. 1, 2018, pp. 410–450. https://doi.org/10.2514/1.C034442.

[2] Garrigues, E., "A Review of Industrial Aeroelasticity Practices at Dassault Aviation," Journal of Aerospace Lab, Vol. 14, 2018, pp. 1–34. https://doi.org/10.12762/2018.AL14-09.

[3] Murua, J., Martínez, P., Climent, H., van Zyl, L., and Palacios, R., "T-tail flutter: Potential-flow modelling, experimental validation and flight tests," Progress in Aerospace Sciences, Vol. 71, 2014, pp. 54–84. https://doi.org/https://doi.org/10.1016/j.paerosci.2014.07.002.

[4] Livne, E., and Weisshaar, T. A., "Aeroelasticity of nonconventional airplane configurations - Past and future," Journal of Aircraft, Vol. 40, No. 6, 2003, pp. 1047–1065. https://doi.org/10.2514/2.7217.

[5] Su, W., and Cesnik, C. E. S., "Nonlinear Aeroelasticity of a Very Flexible Blended-Wing-Body Aircraft," Journal of Aircraft, Vol. 47, No. 5, 2010, pp. 1539–1553. https://doi.org/10.2514/1.47317.

[6] Cook, R. G., Calderon, D. E., Cooper, J. E., Lowenberg, M. H., and Neild, S. A., "Industrially inspired gust loads analysis of various-aspect-ratio wings featuring geometric nonlinearity," Journal of Aircraft, Vol. 57, No. 1, 2020, pp. 13–28. https://doi.org/10.2514/1.C035294.

[7] Bradley, M. K., and Droney, C. K., "Subsonic Ultra Green Aircraft Research: Phase I Final Report," Tech. rep., NASA CR-2011-21, 2011. URL https://ntrs.nasa.gov/citations/20110011321.

[8] Cesnik, C. E., Palacios, R., and Reichenbach, E. Y., "Reexamined structural design procedures for very flexible aircraft," Journal of Aircraft, Vol. 51, No. 5, 2014, pp. 1580–1591. https://doi.org/10.2514/1.C032464.

[9] Calderon, D. E., Cooper, J. E., Lowenberg, M., Neild, S. A., and Coetzee, E. B., "Sizing high-aspect-ratio wings with a geometrically nonlinear beam model," Journal of Aircraft, Vol. 56, No. 4, 2019, pp. 1455–1470. https://doi.org/10.2514/1.C035296.

[10] Murua, J., Palacios, R., and Graham, J. M. R., "Applications of the unsteady vortex-lattice method in aircraft aeroelasticity and flight dynamics," Progress in Aerospace Sciences, Vol. 55, 2012, pp. 46–72. https://doi.org/10.1016/j.paerosci.2012.06.001.

[11] Kim, T., "Flutter prediction methodology based on dynamic eigen decomposition and frequency-domain stability," Journal of Fluids and Structures, Vol. 86, 2019, pp. 354–367. https://doi.org/10.1016/j.jfluidstructs.2019.01.022.

[12] Otsuka, K., Wang, Y., and Makihara, K., "Three-dimensional aeroelastic model for successive analyses of high-aspect-ratio wings," Journal of Vibration and Acoustics, Transactions of the ASME, Vol. 143, No. 6, 2021. https://doi.org/10.1115/1.4050276.

[13] Jonsson, E., Riso, C., Lupp, C. A., Cesnik, C. E., Martins, J. R., and Epureanu, B. I., "Flutter and post-flutter constraints in aircraft design optimization," Progress in Aerospace Sciences, Vol. 109, No. April, 2019, p. 100537. https://doi.org/10.1016/j.paerosci.2019.04.001.

[14] Bartels, R. E., Funk, C. J., and Scott, R. C., "Limit-cycle oscillation of the Subsonic Ultra-Green Aircraft Research Truss-Braced Wing aeroelastic model," Journal of Aircraft, Vol. 54, No. 5, 2017, pp. 1605–1613. https://doi.org/10.2514/1.C034064.

[15] Mallik, W., Schetz, J. A., and Kapania, R. K., "Rapid transonic flutter analysis for aircraft conceptual design applications," AIAA Journal, Vol. 56, No. 6, 2018, pp. 2389–2402. https://doi.org/10.2514/1.J056218.

[16] Riso, C., Ghadami, A., Cesnik, C. E., and Epureanu, B. I., "Data-driven forecasting of postflutter responses of geometrically nonlinear wings," AIAA Journal, Vol. 58, No. 6, 2020, pp. 2726–2736. https://doi.org/10.2514/1.J059024.

[17] Denegri, C. M., Dubben, J. A., and Maxwell, D. L., "In-flight wing deformation characteristics during limit-cycle oscillations," Journal of Aircraft, Vol. 42, No. 2, 2005, pp. 500–508. https://doi.org/10.2514/1.1345.

[18] Denegri, C. M., Sharma, V. K., and Northington, J. S., "F-16 limit-cycle oscillation analysis using nonlinear damping," Journal of Aircraft, Vol. 53, No. 1, 2016, pp. 243–250. https://doi.org/10.2514/1.C033315.

[19] Denegri, C. M., Sharma, V. K., and Neergaard, L. J., "Experimental characterization of nonlinear damping in the f-16 wing structure," Journal of Aircraft, Vol. 58, No. 2, 2021, pp. 236–243. https://doi.org/10.2514/1.C035850.

[20] Pace, D. K., "Fidelity, Resolution, Accuracy, and Uncertainty," Modeling and Simulation in the Systems Engineering Life Cycle, edited by M. L. Loper, Springer, 2015, Chap. 3, pp. 29–39. https://doi.org/10.1007/978-1-4471-5634-5_28.

[21] del Carre, A., Teixeira, P., Palacios, R., and Cesnik, C. E., "Nonlinear response of a very flexible aircraft under lateral gust," International Forum on Aeroelasticity and Structural Dynamics, Savannah, Georgia, USA, 2019. URL https://www.asdjournal.org/public/Proceedings/IFASD_2019/IFASD-2019-090.pdf.

[22] Hollowell, S. J., and Dugundji, J., "Aeroelastic flutter and divergence of stiffness coupled, graphite/epoxy cantilevered plates," Journal of Aircraft, Vol. 21, No. 1, 1984, pp. 69–76. https://doi.org/10.2514/3.48224.

[23] Landsberger, B. J., and Dugundji, J., "Experimental aeroelastic behavior of unswept and forward-swept cantilever graphite/epoxy wings," Journal of Aircraft, Vol. 22, No. 8, 1985, pp. 679–686. https://doi.org/10.2514/3.45186.

[24] Tang, D., and Dowell, E. H., "Experimental and theoretical study on aeroelastic response of high-aspect-ratio wings," AIAA Journal, Vol. 39, No. 8, 2001, pp. 1430–1441. https://doi.org/10.2514/2.1484.

[25] Tang, D., and Dowell, E. H., "Experimental and Theoretical Study on Aeroelastic Response of High-Aspect-Ratio Wings," AIAA Journal, Vol. 39, No. 8, 2001, pp. 1430–1441. https://doi.org/10.2514/2.1484.

[26] Tang, D., and Dowell, E. H., "Limit-cycle hysteresis response for a high-aspect-ratio wing model," Journal of Aircraft, Vol. 39, No. 5, 2002, pp. 885–888. https://doi.org/10.2514/2.3009.

[27] Tang, D., and Dowell, E. H., "Aeroelastic analysis and experiment for wing/store model with stiction nonlinearity," Journal of Aircraft, Vol. 48, No. 5, 2011, pp. 1512–1530. https://doi.org/10.2514/1.C031151.

[28] Britt, R. T., Ortega, D., McTigue, J., and Scott, M. J., "Wind tunnel test of a very flexible aircraft wing," 53rd AIAA/ASME/ASCE/AHS/ASC Structures, Structural Dynamics and Materials Conference, 2012, pp. 1–24. https://doi.org/10.2514/6.2012-1464.

[29] Avin, O., Drachinsky, A., Ben Shmuel, Y., Raveh, D. E., and Tur, M., "An Experimental Benchmark of a Very Flexible Wing," AIAA Scitech Forum, Nashville, Tennessee, USA, 2021. https://doi.org/10.2514/6.2021-1709.

[30] Afonso, F., Coelho, M., Vale, J., Lau, F., and Suleman, A., "On the design of aeroelastically scaled models of high aspect-ratio wings," Aerospace, Vol. 7, No. 11, 2020, pp. 1–18. https://doi.org/10.3390/aerospace7110166.

[31] del Carre, A., Muñoz-Simón, A., Goizueta, N., and Palacios, R., "SHARPy : A dynamic aeroelastic simulation toolbox for very flexible aircraft and wind turbines," Journal of Open Source Software, Vol. 4, No. 44, 2019, p. 1885. https://doi.org/10.21105/joss.01885.

[32] Hesse, H., Palacios, R., and Murua, J., "Consistent structural linearisation in flexible aircraft dynamics with large rigid-body motion," AIAA Journal, Vol. 52, No. 3, 2014, p. 528. https://doi.org/10.1016/j.compstruc.2012.05.011.

[33] Maraniello, S., and Palacios, R., "Parametric Reduced-Order Modeling of the Unsteady Vortex-Lattice Method," AIAA Journal, Vol. 58, No. 5, 2020, pp. 2206–2220. https://doi.org/10.2514/1.j058894.

[34] Goizueta, N., Wynn, A., and Palacios, R., "Parametric Krylov-based order reduction of aircraft aeroelastic models," AIAA Scitech Forum, Nashville, Tennessee, USA, 2021. https://doi.org/10.2514/6.2021-1798.

[35] del Carre, A., Goizueta, N., Muñoz-Simón, A., and Palacios, R., "SHARPy: A dynamic aeroelastic simulation toolbox for very flexible aircraft and wind turbines," , Feb. 2021. https://doi.org/10.5281/zenodo.4522202.

[36] Geradin, M., and Cardona, A., Flexible multibody dynamics: a finite element approach, John Wyley and Sons, Chichester, 2001.

[37] Simpson, R. J. S., and Palacios, R., "Numerical aspects of nonlinear flexible aircraft flight dynamics modeling," 54th AIAA/ASME/ASCE/AHS/ASC Structures, Structural Dynamics, and Materials Conference, Boston, Massachusetts, USA, 2013. https://doi.org/10.2514/6.2013-1634.

[38] Katz, J., and Plotkin, A., "Unsteady Incompressible Potential Flow," Low Speed Aerodynamics, Cambridge University Press, 2001, Chap. 13, 2nd ed., pp. 369–433. https://doi.org/10.1017/CBO9780511810329.

[39] Del Carre, A., and Palacios, R., "Low-Altitude Dynamics of Very Flexible Aircraft," AIAA Scitech Forum, San Diego, California, USA, 2019, pp. 1–20. https://doi.org/10.2514/6.2019-2038.

[40] Simpson, R. J. S., Palacios, R., and Murua, J., "Induced-Drag Calculations in the Unsteady Vortex Lattice Method," AIAA Journal, Vol. 51, No. 7, 2013, pp. 1775–1779. https://doi.org/10.2514/1.j052136.

[41] Maraniello, S., and Palacios, R., "State-Space Realizations and Internal Balancing in Potential-Flow Aerodynamics with Arbitrary Kinematics," AIAA Journal, Vol. 57, No. 6, 2019, pp. 1–14. https://doi.org/10.2514/1.J058153.

[42] Artola, M., Goizueta, N., Wynn, A., and Palacios, R., "Modal-Based Nonlinear Estimation and Control for Highly Flexible Aeroelastic Systems," AIAA Scitech Forum, Orlando, Florida, USA, 2020. https://doi.org/10.2514/6.2020-1192.

[43] Drachinsky, A., and Raveh, D. E., "Modal Rotations: A Modal-based Method for Large Structural Deformations," AIAA Journal, Vol. 58, No. 7, 2020, pp. 3159–3173. https://doi.org/10.2514/1.J058899.

[44] Drachinsky, A., and Raveh, D. E., "Nonlinear Aeroelastic Analysis of Highly Flexible Wings Using the Modal Rotation Method," AIAA Journal, 2021. https://doi.org/10.2514/1.J061065, Article in Advance.

[45] Su, W., and Cesnik, C. E. S., "Strain-Based Analysis for Geometrically Nonlinear Beams: A Modal Approach," Journal of Aircraft, Vol. 51, No. 3, 2014, pp. 890–903. https://doi.org/10.2514/1.C032477.

[46] Riso, C., and Cesnik, C. E. S., "Correlations Between UM/NAST Nonlinear Aeroelastic Simulations and the Pre-Pazy Wing Experiment," AIAA Scitech Forum, Nashville, Tennessee, USA, 2021. https://doi.org/10.2514/6.2021-1712.

[47] Artola, M., Wynn, A., and Palacios, R., "Generalized Kelvin–Voigt damping for geometrically nonlinear beams," AIAA Journal, Vol. 59, No. 1, 2021, pp. 356–365. https://doi.org/10.2514/1.J059767.

[48] Kareem, A., and Gurley, K., "Damping in structures: Its evaluation and treatment of uncertainty," Journal of Wind Engineering and Industrial Aerodynamics, Vol. 59, No. 2-3, 1996, pp. 131–157. https://doi.org/10.1016/0167-6105(96)00004-9.

[49] Gao, G., and Zhu, L., "Nonlinearity of mechanical damping and stiffness of a spring-suspended sectional model system for wind tunnel tests," Journal of Sound and Vibration, Vol. 355, 2015, pp. 369–391. https://doi.org/10.1016/j.jsv.2015.05.033.

[50] Zaero Theoretical Manual V. 9.2, Scottsdale, AZ, 3rd ed., 2017.

[51] Avin, O., Drachinsky, A., Ben-Shmuel, Y., and Raveh, D. E., "Design of an Experimental Benchmark of a Highly Flexible Wing," 60th Israel Annual Conference on Aerospace Sciences, 2020.

[52] Chen, P. C., Lee, H. W., and Liu, D., "Unsteady subsonic aerodynamics for bodies and wings with external stores including wake effect," Journal of Aircraft, Vol. 30, No. 5, 1993, pp. 618–628. https://doi.org/10.2514/3.46390.

[53] Chen, P. C., "Damping perturbation method for flutter solution: The g-method," AIAA Journal, Vol. 38, No. 9, 2000, pp. 1519–1524. https://doi.org/10.2514/2.1171.

[54] Drachinsky, A., and Raveh, D. E., "Nonlinear Aeroelastic Analysis of Highly Flexible Wings Using the Modal Rotation Method," AIAA Scitech Forum, Nashville, Tennessee, USA, 2021. https://doi.org/10.2514/6.2021-1710.

[55] Drachinsky, A., Avin, O., Raveh, D. E., Ben-Shmuel, Y., and Tur, M., "Flutter Tests of the Pazy Wing," Accepted for publication in AIAA SciTech Forum, 2022.

[56] Bunton, R. W., and Denegri, C. M., "Limit cycle oscillation characteristics of fighter aircraft," Journal of Aircraft, Vol. 37, No. 5, 2000, pp. 916–918. https://doi.org/10.2514/2.2690.